Correcting Swath-Dependent Bias of MODIS FRP Observations With Quantile Mapping

Inderpreet Kaur [1], **Imke Hüser** [1], **Tianran Zhang** [2], **Berit Gehrke** [1] **and Johannes W. Kaiser** [1,3,*]

[1] Department of Atmospheric Chemistry, Max Planck Institute for Chemistry (MPIC), 55128 Mainz, Germany; i.kaur@mpic.de (I.K.); imke.hueser@mpic.de (I.H.); b.gehrke@mpic.de (B.G.)
[2] Department of Geography, King's College London (KCL), London WC2B4BG, UK; tianran.zhang@kcl.ac.uk
[3] Deutscher Wetterdienst (DWD), 63067 Offenbach am Main, Germany
[*] Correspondence: johannes.kaiser@dwd.de

Abstract: Active fire observations with satellite instruments exhibit a well-documented increase of the detection threshold with increasing pixel footprint size, i.e., distance from the sub-satellite point. This results in a viewing angle-dependent, negative bias in gridded representations of the observed Fire Radiative Power (FRP), which in turn is frequently being used for climate monitoring of biomass burning and for pyrogenic emission inventories. We present a method based on quantile mapping to alleviate this bias and apply it to the gridded-FRP from the Moderate Resolution Imaging Spectroradiometer (MODIS) satellite instruments. The gridded-FRP observations are corrected with a correction function that depends on the satellite viewing angle and the magnitude of FRP in each grid cell. Assuming the fire observations at *nadir* to be the best representation of the truth, we derive a correction function by mapping cumulative distribution function (CDF) of *off-nadir* gridded-FRP to the CDF of *near-nadir* gridded-FRP. The method can be directly applied to correct the negative bias in gridded-FRP observations at a grid resolution of 1° or more. The performance of the correction methodology is confirmed through comparisons with co-located Visible Infrared Imaging Radiometer Suite (VIIRS) satellite observations: After bias correction, the gridded-FRP observations from both satellites agree better than before, particularly over savanna, tropical forests, and extra-tropical forests. Experiments with the Global Fire Assimilation System (GFAS) show that the impacts of the bias-corrected MODIS/Aqua gridded-FRP observations and VIIRS/Suomi-NPP gridded-FRP observations on regional FRP analyses are comparable, which confirms the potential for improving fire emission inventories and climate monitoring based on FRP.

Keywords: Fire Radiative Power (FRP); Moderate Resolution Imaging Spectroradiometer (MODIS); viewing angle dependence; quantile mapping bias correction

1. Introduction

Satellite-based active fire observation is important for monitoring fires and their emissions. The Moderate Resolution Imaging Spectroradiometer (MODIS) instruments aboard NASA's Aqua and Terra satellites have been providing different active fire and thermal anomaly products for two decades [1]. Fire radiative power (FRP) is an important active fire characteristic which is used in various fire emission inventories [2–6]. The estimates from emission inventories are used in regional and global atmospheric composition models for real-time air-quality monitoring and long-term climate studies. Unfortunately, the inherent limitations of the MODIS instruments introduce a spurious variability in the observations which in turn affects the performance of the model outputs: the fire detection threshold of MODIS instruments increases with the increasing pixel size towards the swath

edges, thus the small fires with magnitudes below the detection limit are not detected. The missing fires introduce an underestimation in FRP-based biomass burning inventories like the 'Global Fire Assimilation System (GFAS)' for grid cells that are observed off-nadir or even near the swath edges.

The MODIS instruments provide global coverage of various geophysical parameters, including active fire products. Terra and Aqua scan the Earth at 1030/2230 h and 1330/0130 h local solar time respectively and provide global coverage every 1–2 days, while the viewing geometry of MODIS repeats every 16 days. The MODIS Level 2 active fire products cover an area of 2340 km × 2030 km in the along-scan and along-track directions, respectively, with a pixel area of 1 km^2 at nadir. The fine spatial resolution of the MODIS instruments is capable of detecting smaller/cooler fires more effectively than its geostationary counterparts. However, due to the scan geometry and the earth's curvature, similar performance cannot be expected over the entire MODIS swath. Towards the swath edges, the MODIS scan geometry and the earth's curvature introduce a bow-tie effect and the pixel sizes get larger [7]. The bow-tie effect leads to an increase in the scan-to-scan overlap, thus introducing duplicate detections of the same fire in consecutive scans [8]. At the swath edges, the pixel area is approximately 9 km^2 [8]. The increase in the pixel area towards the swath edges causes a fire of given magnitude to occupy a decreasing fraction of the pixel. This leads to a higher detection threshold at swath edges. All fires with magnitude less than the detection threshold are not detected by the MODIS instruments. Freeborn et al. [8] analyse the MODIS/Aqua fire detections over Africa and show that a fire has to be at least eight times stronger than at nadir to be successfully detected by MODIS at the swath edges. Similarly, a study by Zhang et al. [9] over Eastern China agricultural fires shows that the minimum per-pixel FRP (Appendix A) successfully detected at approximately 60° MODIS viewing angle is 12 times stronger than at nadir.

The missing fire detections have two distinct effects when aggregated on a grid in FRP inventories like Global Fire Assimilation System (GFAS) [2]. Firstly, when these *missing fire* pixels have no active fire pixels in the neighbourhood, an aggregation on a grid results in "false zero" grid cells. It should be noted that the grid cells with no fire-activity are interpreted as "true" observations of no-fire. Secondly, when the *missing fire* pixels are aggregated with neighbouring non-zero fire pixels, the FRP in that grid cell is underestimated. Both these effects when combined with the MODIS observational frequency introduces a spurious fluctuation in the GFAS FRP analyses.

The MODIS instruments approximately observe the same area alternatively at nadir and off-nadir, thus detecting the same fire activity at different detection thresholds. If the fire activity is a cluster, the small fires are alternatively "detected" and "missed" in MODIS overpasses. These false gaps in the time series introduces a spurious oscillation in the GFAS FRP analyses, particularly in regions of widespread small fire activity. For example, Andela et al. [10] show for GFAS FRP analyses, that fire clusters spread over 100 km in sub-Saharan Africa have a spurious oscillation with a period of approximately two days. When emission estimates from the biased GFAS FRP analyses are assimilated, the errors propagate to the regional and global transport models. For example, Saide et al. [11] show for the Rim fire, California in 2013, that the emission estimates from WRF-Chem have a poor correlation with the burnt area estimates due to improper representation of day-to-day variability in MODIS gridded-FRP observations. Other factors like characterisation of diurnal cycle variability in FRP inventories and attenuation of the signal of near-infrared (NIR) bands by smoke can also contribute to errors in emission estimates, but we do not address these issues in this study.

For a more accurate utilisation of the MODIS FRP observations in various emission monitoring and forecasting systems, a proper characterization of the inconsistencies is essential. In the past, a few studies have tried to correct this bias through different approaches. For example, Freeborn et al. [8] derive bow-tie adjustment factors by fitting the symmetrical along-scan profiles of FRP observations over Africa, from Terra and Aqua, as second order polynomials. In another study, Andela et al. [12] calibrate the MODIS Fire Radiative Energy (FRE) observations against the field measurements over Africa and find that a correction factor of 1.56 is needed to compensate for the sensor limitations. While Wang et al. [13] empirically correct the underestimation of the FRP-based emissions over

northern sub-Saharan Africa by assuming persistence within regional burn patterns over small-scale homogeneous areas. However, in all these studies, the bias correction approach is derived from MODIS FRP observations over large biomass burning areas like Africa, which hinders its application to FRP observations on smaller and global scales. The sensor limitation significantly affects the smaller fires, e.g., agricultural waste burning [14], and a separate analysis for each fire type is necessary.

Kaiser et al. [15] have shown that the underestimation in gridded MODIS FRP at large viewing angles has a pronounced dependence on the land cover type. This indicates that the underestimation is intrinsically dependent on the fire type. Therefore, in this study, we present a correction methodology characterised by the fire type/magnitude and the viewing angle. This correction procedure provides a grid-level mitigation of the swath-dependent bias, and is applicable to MODIS gridded-FRP in various emission inventories. Finally, in order to evaluate the efficiency of the methodology, we assess the similarities and differences between the gridded-FRP from Visible Infrared Imaging Radiometer Suite (VIIRS) Suomi National Polar-orbiting Partnership (Suomi-NPP) and the bias adjusted MODIS gridded-FRP.

2. Data and Methods

2.1. Input Data

In this study, we use Collection 6 MOD14 (Terra) and MYD14 (Aqua) MODIS fire products [16] (https://earthdata.nasa.gov/earth-observation-data/near-real-time/firms/active-fire-data). The MODIS products use brightness temperatures from 4 μm, 11 μm, and 12 μm channels for active fire detection and reflectance from 0.65 μm, 0.86 μm, and 2.1 μm channels for coastal false alarm rejection, sun-glint mask, and cloud mask [17]. The Collection 6 MODIS active fire detection algorithm identifies any burning pixels in each MODIS granule. The MODIS pixels are classified as: (i) missing data, (ii) cloudy, (iii) non-fire, (iv) fire, or (v) unknown [17]. The two MODIS instruments provide four daily active fire observation products, called MOD14 and MYD14.

The MODIS active fire products MOD14 and MYD14 are observations of FRP in units of Watt per pixel p. These per-pixel FRP (frp_p) values are re-scaled on a global 0.1° grid using the GFAS gridding algorithm. The GFAS gridding algorithm is an update of the methodology described in [2]. It aggregates all individual per-pixel FRP values that belong to grid cell q, to obtain the FRP areal density

$$\rho_q = \frac{\sum_{p \in q} frp_p}{\sum_{p \in q} A_p} \tag{1}$$

where A_p is the individual pixel area of any per-pixel FRP of MODIS, either fire or non-fire. The FRP areal density has units of W m^{-2}. The oversampling of fires due to the bow-tie effect has no effect on FRP areal density because multiple observations of the same fire are summed in the same way as multiple observations of non-burning areas. The per-pixel FRP from all MODIS granules within a one-hour window are gridded to their corresponding latitude/longitude grid cell. This results in a global gridded FRP areal density field with a temporal resolution of one hour. Multiplying the FRP areal density (Equation (1)) with the grid cell area δ_q results in the FRP observed per 0.1° grid cell in Watt, referred to as 'gridded-FRP'

$$\varrho_q = \rho_q * \delta_q \tag{2}$$

For more details on the gridding methodology see Nikonovas et al. [18].

2.2. Quantile Mapping

Quantile mapping (QM) is frequently used to correct systematic stationary biases associated with modelled quantities [19–21]. QM seeks to project the shape of the cumulative distribution function (CDF) of a modelled variable onto the distribution of an observed quantity. Let x_o be the set containing all the observations, and x_m be the set of modeled quantities. If the CDF of the modelled quantity and

the observed quantity are $F_m(x_m)$ and $F_{\text{obs}}(x_o)$, respectively, then the two distributions should overlap if no bias exists between them:

$$F_{\text{obs}}(x_o) = F_m(x_m) \tag{3}$$

If the CDFs are invertible, a transfer function can be used to re-calculate modelled quantities $\hat{x}_m$, such that their distribution matches the distribution of the observed quantities

$$\hat{x}_m = F_{\text{obs}}^{-1}(F_m(x_m)) \tag{4}$$

In this study, we determine the CDF empirically, though a parametric distribution can also be chosen for other problems.

2.3. QM Adjustment

2.3.1. Overview

The correction procedure presented in this study is based on the assumption that, if MODIS instruments are devoid of any bias, the observed frequency-magnitude distributions of gridded-FRP should be identical at different viewing angles. However, the underestimation in the gridded-FRP at large viewing angles introduces differences between the frequency-magnitude distributions at different viewing angles. We use quantile mapping, as described in the previous section, to remove the bias. We select grid cells with viewing angles close to nadir as a proxy for the observation set x_o and grid cells with off-nadir nadir viewing angles as x_m. The transfer function re-calculates the *off-nadir* gridded-FRP $\hat{x}_m$ such that its CDF matches the CDF of *near-nadir* gridded-FRP. The resulting ratio of the corrected gridded-FRP to the uncorrected gridded-FRP is the correction factor required to compensate the bias.

With this approach, the grid cells with non-zero observations can be corrected, but grid cells with "false zero" observations cannot be compensated. We therefore propose an indirect way for compensating this gap by calculating the correction factors at a coarser resolution. When the gridded-FRP observations are re-gridded on a coarser resolution, the probability of gridding a "missed fire" with an "observed fire" in the vicinity is higher, thus decreasing the number of "false zero" grid cells. As vegetation fires occur in clusters, we assume that there exists a spatial resolution where it is possible to grid a significant part of the "false zero" detections with other non-zero detections in the neighbourhood.

This assumption is based on Kaiser and Heil [22], who compare the histograms of co-located MODIS *near-nadir* gridded-FRP and SEVIRI gridded-FRP at different resolutions. They observe that the number of missing fire detections falls rapidly with decreasing resolution, and that the fall is more rapid between 0.1° and 1°. A further decrease in resolution only slightly alters the total number of missing detections. In our analysis, it is not possible to examine such paired observations, thus in order to deduce a spatial resolution suitable for bias correction, we determine and analyse the correction factors for three spatial resolutions, i.e., 0.1°, 1°, and 2°.

2.3.2. Correction Factors

The gridded-FRP observations from both MODIS instruments for each 1-hour time slot of 2016 are chosen as control data. The correction factors derived from these observations are used to correct the MODIS gridded-FRP from other years. A detailed description of the steps involved in deriving the correction factors is described below:

1. The gridded FRP observations from both MODIS instruments are grouped in 50 logarithmically spaced intervals (*j*) ranging from $\varrho_1 = 1\,\text{MW}$ to $\varrho_{50} = 50\,\text{GW}$ and 10 unequally spaced viewing angle intervals (*i*) in the interval 0° to 65°. The viewing angles bins are selected such that each angular bin has a 150 km wide field of view. The grid cells with viewing angle less than 12°

(equivalent to first 150 km of the swath) are chosen as the representation of nadir. Other grid cells with viewing angles greater than 12° are considered as off-nadir observations.

2. To include contribution from the non-fire grid cells and "missed detections", the total number of grid cells with zero magnitude are also calculated and added to the first FRP bin, for each viewing angle bin.

3. If $n_{i,j}$ is the number of grid cells with viewing angle θ in viewing angle bin i and FRP ϱ in FRP bin j, then the probabilities of observations in the FRP and viewing angle bins are described by the following probability density function (PDF)

$$PDF_i\left(\lg \varrho_j\right) = \frac{1}{\lg \varrho_{j+1} - \lg \varrho_j} \times \frac{n_{i,j}}{\sum_{j'=1}^{J} n_{i,j'}} . \tag{5}$$

where J = 50 is the number of FRP bins. The PDFs are not needed in the correction method but will be shown to illustrate and confirm that the method works as expected.

The average observed FRP in each viewing angle bin is

$$\bar{\varrho}_i = \sum_{j=1}^{J} \frac{\varrho_j + \varrho_{j+1}}{2} \times \frac{n_{i,j}}{\sum_{j'=1}^{J} n_{i,j'}} \tag{6}$$

This quantity will be used to assess the the effectiveness of the bias removal at different spatial resolutions.

4. As the probability of detecting a fire decreases with increasing viewing angle, it is more appropriate to use a reverse than a standard cumulative distribution function (CDF). The reverse CDF represents the probability of detecting a fire larger than a given FRP. In this study, it is discretely calculated as

$$F_{i,j} = \frac{\sum_{j'=j}^{J} n_{i,j'}}{\sum_{j'=1}^{J} n_{i,j'}} \tag{7}$$

5. The transfer function maps the CDF for each off-nadir angular bin to the CDF of the first angular bin (nadir) and re-calculates the gridded-FRP observations such that their frequency-distribution matches the frequency-distribution of the *nadir* gridded-FRP. We therefore set:

$$F_{\text{obs}} = F_1 \tag{8}$$
$$x_{\text{obs}} = \varrho_j \tag{9}$$
$$F_{\text{m}} = F_i \tag{10}$$
$$x_{\text{m}} = \varrho_j \tag{11}$$

The corrected FRP $\hat{\varrho}_{i,j}$ is then approximated as the remapped FRP ϱ_j and calculated according to Equation (4):

$$\hat{\varrho}_{i,j} = F_1^{-1}(F_i(\varrho_j)) \tag{12}$$

Mathematically, the transfer function for each off-nadir bin is thus estimated by inverting the CDF of the *nadir* gridded-FRP and using input values from the *off-nadir* CDF. A look-up table of the multiplicative correction factor for each *off-nadir* corrected gridded-FRP is estimated as

$$\zeta_{i,j} = \frac{\hat{\varrho}_{i,j}}{\varrho_j} \tag{13}$$

6.   Finally, we parameterise this discrete look-up table of correction factors $\zeta_{i,j}$ as a continuous function $\zeta(\varrho, \theta)$ of the gridded-FRP magnitude ϱ and the viewing angle θ. In subsequent sections, the term 'correction function' is used to describe the parameterisation of the correction factors.

2.3.3. Spatial Resolution of Correction

We expect that calculating and applying the correction factor on a coarser resolution grid results in a more complete bias removal. However, using a coarser resolution also implies a loss of spatial information on the correction factors, and thus the FRP field. The resolution of the correction factor will therefore need to balance both effects. We examine the suitability of three resolutions, i.e., the original resolution of 0.1° and coarser resolutions of 1° and 2° in two different ways: (1) we calculate the parameterised form of the correction factors and compare how the parameter values change with resolution, and (2) we apply the correction factors at the different resolutions and determine the residual biases of the off-nadir observations.

2.3.4. Application of the Correction Function

Once a suitable spatial resolution has been chosen and the corresponding universal correction function $\zeta(\varrho, \theta)$ has been calculated, all 0.1°-gridded FRP observations (for any hour) are being corrected as follows:

1.   The FRP observation and corresponding viewing angle fields are interpolated conservatively to the coarser resolution.
2.   The appropriate field of correction factors for each coarse grid cell is calculated using the correction function $\zeta(\varrho, \theta)$.
3.   The field of correction factors is interpolated to the finer resolution of 0.1° with the nearest-neighbour method.
4.   The 0.1°-gridded FRP field is multiplied with the correction factor field.

2.4. Validation

To assess the applicability of the correction procedure, the correction function derived from control data (gridded-FRP during 2016) is used to correct the gridded-FRP during 2017.

MODIS and VIIRS Comparison: Due to non-availability of extensive ground data, we compare both uncorrected and corrected MODIS gridded-FRP observations to Visible Infrared Imaging Radiometer Suite (VIIRS) gridded-FRP observations from the year 2017.

The VIIRS instrument aboard the joint NASA/NOAA Suomi National Polar-orbiting Partnership (Suomi-NPP) satellite provides an active fire product with a spatial resolution of 750 m (https://earthdata.nasa.gov/earth-observation-data/near-real-time/firms/viirs-i-band-active-fire-data). The VIIRS pixels are generated using an on-board aggregation scheme which limits the growth rate of the VIIRS pixel with respect to the viewing angle. Hence the VIIRS detection threshold is more or less similar across the swath. A slight dependency can be expected at the swath edge, where the VIIRS pixel size is almost twice its size at nadir [23], though.

Almost similar equatorial crossing times of Aqua and Suomi-NPP provide a comparison of simultaneous FRP detections over the whole globe. Terra and Suomi-NPP simultaneous detections occur only over higher latitudes and are not included in the comparison. The VIIRS active fire pixels are aggregated to the GFAS grid according to the methodology described in Zhang et al. [24]. The grid cells with the fraction of observed area less than 80% are associated with higher uncertainty and are excluded from the comparison. This information is available as '*fraction of observed area*' in the GFAS gridded product. We also exclude grid cells with magnitude above 10 GW because a smaller number observations with such high magnitude does not allow for proper statistics. The grid cells with gridded-FRP = 0 are also excluded from the comparison. These null grid cells either represent no fire activity or the part of missing fire detections which cannot be corrected by this method.

Let N_i (index of summation 'n') be the number of eligible MODIS/Aqua and VIIRS/Suomi-NPP collocation pairs in each viewing angle bin i. If $\varrho_M(i,n)$ and $\varrho_V(i,n)$ represent the gridded-FRP for each MODIS and VIIRS collocation pair respectively, the normalized mean bias and normalized root mean square error (NRMSE) for each viewing angle bin is calculated as

$$\text{NRMSE}(i) = \frac{1}{\bar{\varrho}_V(i)} \sqrt{\frac{\sum_{n=1}^{N_i} \left(\varrho_M(i,n) - \varrho_V(i,n)\right)^2}{N_i}} \tag{14}$$

$$\text{normalized mean bias}(i) = \frac{1}{N_i} \frac{\sum_{n=1}^{N_i} \left(\varrho_M(i,n) - \varrho_V(i,n)\right)}{\bar{\varrho}_V(i)}, \tag{15}$$

where $\bar{\varrho}_V(i)$ is the VIIRS average gridded-FRP in each viewing angle bin i. These statistics are estimated for different MODIS viewing angles and land cover classes. The land cover class map is defined according to the dominant fire type in GFEDv3.1 [25] and is classified into eight land cover classes: savanna (SA), savanna with organic soil (SAOS), agriculture (AG), agriculture with organic soil (AGOS), tropical forest (TF), peat (PEAT), extra-tropical forest (EF), and extra-tropical forest with organic soil (EFOS) [2].

Effect on GFAS analysis: Finally, in order to assess the effect of the bias-corrected gridded-FRP observations on GFAS "analyses", we perform four experiments with GFAS. These experiments are listed in Table 1. In the experiment 'mm00', gridded-FRP observations from both Terra and Aqua are used, while in experiment 'mv00', gridded-FRP observations from VIIRS/Suomi-NPP are used instead of MODIS/Aqua. The experiments 'mmC0' and 'mvC0' are identical to 'mm00' and 'mv00', but in both the corresponding MODIS gridded FRP observations are bias corrected. In all the experiments, the input gridded-FRP is assimilated every hour to obtain the best estimate of the FRP analyses at each hourly time step. The input data in all four experiments is from the year 2017.

Table 1. Overview of different experiments with Global Fire Assimilation System (GFAS). The column *FRP observations* (Fire Radiative Power) describes the input from different satellite platforms. The suffix "corrected" refers to observations after bias correction. Abbreviations: MOD = Moderate Resolution Imaging Spectroradiometer (MODIS)/Terra, MYD = MODIS/Aqua, VNP = Visible Infrared Imaging Radiometer Suite (VIIRS)/Suomi National Polar-orbiting Partnership (Suomi-NPP).

Experiment ID	FRP Observations	Description
mm00	MOD, MYD	Uncorrected gridded-FRP from MODIS/Aqua and MODIS/Terra are used as input.
mv00	MOD, VNP	Uncorrected gridded-FRP from MODIS/Terra and VIIRS/Suomi-NPP are used as input. VIIRS/Suomi-NPP is used as a replacement for MODIS/Aqua.
mmC0	MOD-corrected, MYD-corrected	Corrected gridded-FRP from both MODIS/Aqua and MODIS/Terra are used as input.
mvC0	MOD-corrected, VNP	Corrected gridded-FRP from MODIS/Terra and gridded-FRP from VIIRS/Suomi-NPP are used as input.

3. Results

3.1. Correction Function

The correction factors derived from MODIS gridded-FRP observations of 1° resolution are depicted by dots in Figure 1. The correction factors for 0.1° and 2° resolution also have similar shape, and are not shown. For each viewing angle bin, the correction factors appear to be made up of two straight lines in log-log space, and thus can be parametrised as

$$\zeta(\varrho, \theta) = 1 + \exp(a - b \log \varrho) + \exp(c - d \log \varrho) . \tag{16}$$

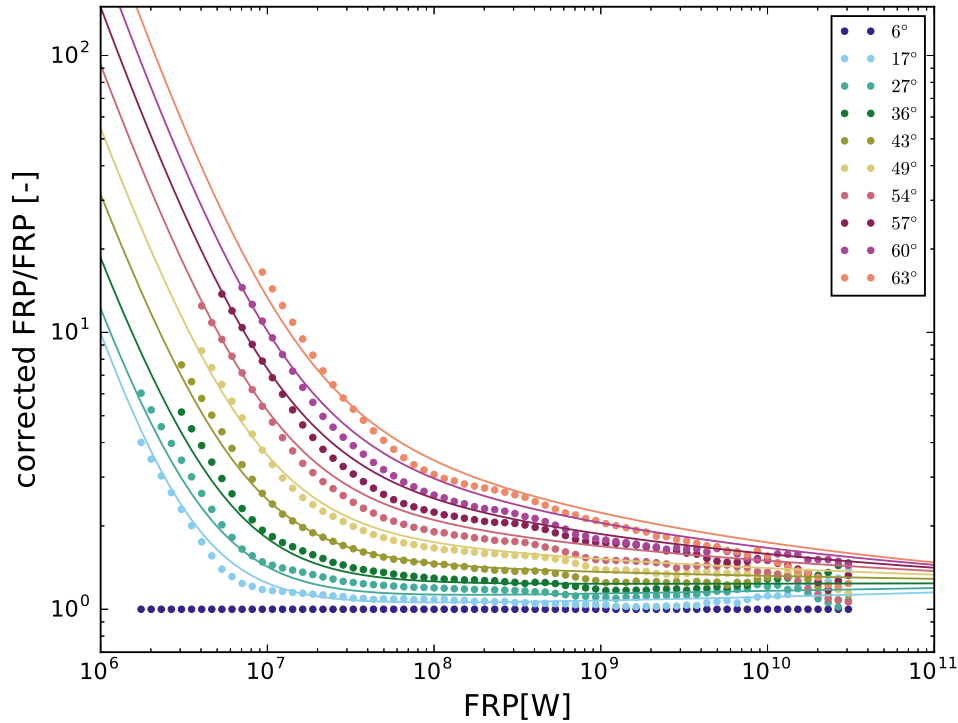where the parameters *a-d* still depend on the viewing angle θ.

Figure 1. The correction factors derived after mapping the cumulative distribution function (CDF) of the *off-nadir* and *nadir* gridded-Fire Radiative Power (FRP) observations from 2016 and at 1° spatial resolution. The dots represent the discrete correction factors $\zeta_{i,j}$ while the lines depict the continuous correction function $\zeta(\varrho, \theta)$ for each viewing angle. The discrete correction factors $\zeta_{i,j}$ can also be used as a look-up table.

A least-squares fit to the discretised correction factors for 0.1° resolution results in the following parameter set:

$$a = 77.7747 - 0.9981\,\theta + 1.3283 \times 10^{-2}\,\theta^2 \tag{17}$$

$$b = 28.6888 - 0.3683\,\theta + 4.576 \times 10^{-3}\,\theta^2 \tag{18}$$

$$c = 254.1455 - 28.0987\,\theta + 1.04731\,\theta^2 - 1.6331 \times 10^{-2}\,\theta^3 + 9.19333 \times 10^{-5}\,\theta^4 \tag{19}$$

$$d = 128.1236 - 13.6775\,\theta + 0.50429\,\theta^2 - 7.824 \times 10^{-3}\,\theta^3 + 4.38171 \times 10^{-5}\,\theta^4 \ , \tag{20}$$

while a different parameter set is found for 1° and 2° resolution:

$$a = 72.76 - 0.677\,\theta + 0.00963\,\theta^2 \tag{21}$$

$$b = 26.83 - 0.248\,\theta + 0.00317\,\theta^2 \tag{22}$$

$$c = -19.43 + 0.54\,\theta \tag{23}$$

$$d = -5.34 + 0.16\,\theta \tag{24}$$

It is interesting to note that the correction functions for both 1° and 2° resolution can be parametrised by the same set of coefficients. However, for 0.1° resolution a higher-order polynomial is required to define the coefficients. This is an indication that the bias correction also works well at 1° and 2° but less so at 0.1°.

The discrete correction factors can be used as a look up table, but using a correction function allows the user to interpolate between discrete viewing angle bins and FRP bins.

3.2. Spatial Resolution of Correction

In the absence of extensive ground based observations, we compare the average gridded-FRP $\bar{\varrho}_i$ in each viewing angle bin i from Equation (6), before and after correction, for all three spatial resolutions. Figure 2 shows the normalised average gridded-FRP in each viewing angle bin before and after correction for all three resolutions. The gridded-FRP at each resolution are corrected with their respective correction function. The average gridded-FRP in each viewing angle bin is normalised by the average gridded-FRP at nadir (first bin) to determine the residual bias for each off-nadir angular bin.
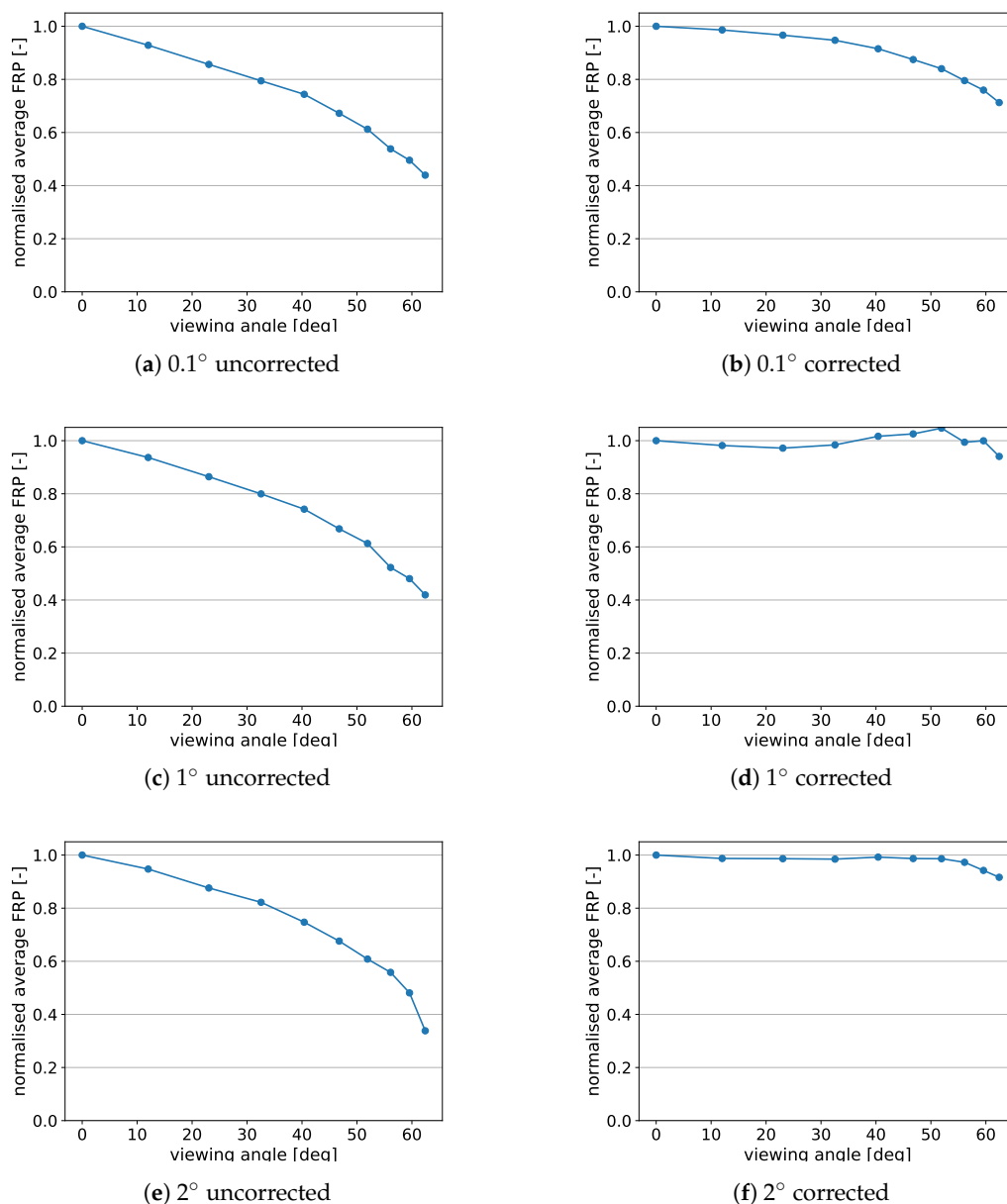

(**a**) 0.1° uncorrected

(**b**) 0.1° corrected

(**c**) 1° uncorrected

(**d**) 1° corrected

(**e**) 2° uncorrected

(**f**) 2° corrected

Figure 2. (**a**,**c**,**e**): The *uncorrected* normalised average gridded-FRP (from control data, year 2016) in each viewing angle bin for 0.1°, 1°, and 2° spatial resolution. (**b**,**d**,**f**): The *corrected* normalised average gridded-FRP in each viewing angle bin for 0.1°, 1°, and 2° grid-level, respectively. The average gridded-FRP in each viewing angle bin is calculated according to Equation (6).

Ideally, over a large sampling period, the average gridded-FRP sensed by Terra and Aqua should be equal in all viewing angle bins. However, due to the increase in the detection threshold at large viewing angles, the average FRP (uncorrected) in each bin is only a fraction of the FRP sensed in the first angular interval. For all three resolutions, more than half of the FRP in the last angular bin belongs to missing or underestimated fires, i.e., the bias is $< -50\%$. After correction at 0.1°, the gridded-FRP bias is reduced at all viewing angles. However, it still reaches -30% for viewing angles greater than 50°. With correction at 1° resolution, the FRP bias is nearly zero for viewing angles less than 40° and becomes slightly positive for viewing angles larger than 40°. Reducing the correction resolution further to 2° removes the slight overestimation, but offers no other significant improvement. At 1° and 2° resolution, the FRP bias which cannot be corrected in the last viewing angle bin is around 6% and 9%, respectively.

The fraction of FRP that goes uncorrected is mostly due to the isolated small fires which have no fire activity in their vicinity. The similar performance of correction functions at 1° and 2° resolution suggests that most of these "false zero" FRP observations have non-zero neighbours within approximately 100 km distance. We conclude that the levels of bias removal of the correction factors derived at 1° and 2° is comparable, which is also in agreement with findings in Kaiser and Heil [22]. Therefore, we choose to work with the former to avoid any unnecessary loss of spatial information. Thus, all the further results presented in this article are based on the correction factors derived at 1° spatial resolution.

3.3. Frequency-Magnitude Distribution of Corrected Gridded-FRP from MODIS

In this section, we illustrate the performance of the correction function towards alleviating the bias in MODIS gridded-FRP observations from 2017 at 1° resolution. Figure 3, *left panel*, shows the number of gridded observations, their corresponding frequency-distribution and CDF, and the contribution to the average gridded-FRP, before any bias correction. The *right panel* shows the corresponding quantities after bias correction. The same statistics for bias corrected 0.1° gridded-FRP fields are provided in the Appendix B.
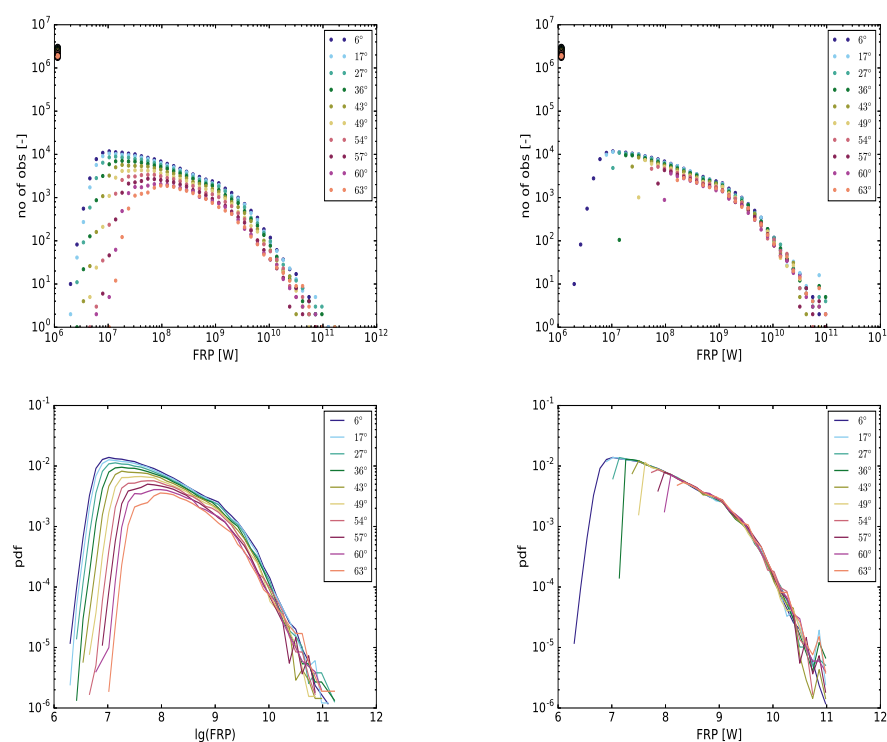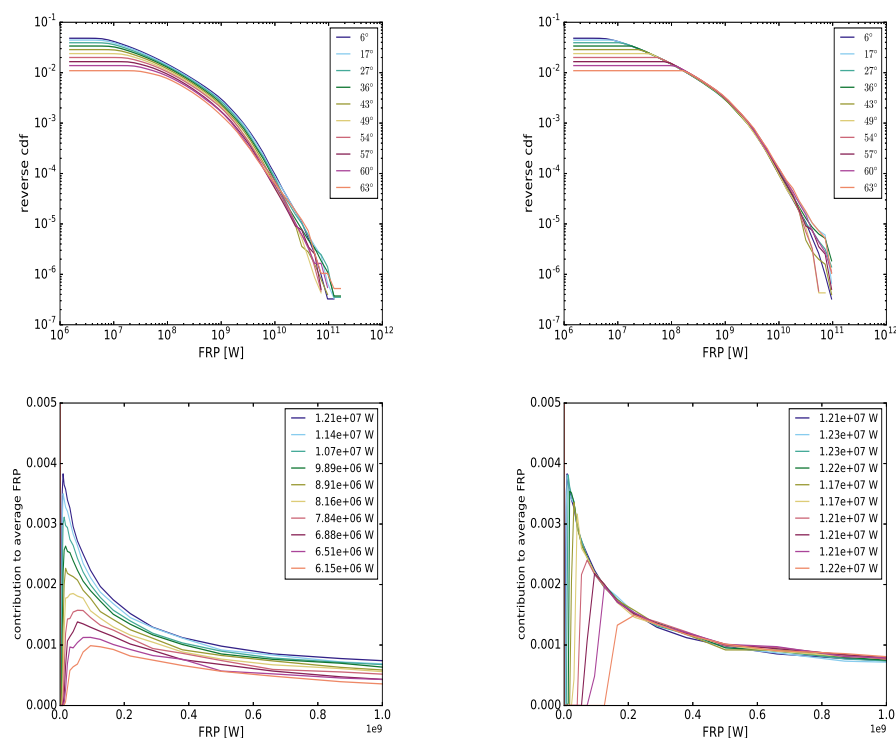

Figure 3. *Cont.*

Figure 3. Statistical properties of Moderate Resolution Imaging Spectroradiometer (MODIS) gridded-FRP observations (hourly, 2017) before and after bias correction. The observations have been corrected according to the correction factors described in Figure 1. The rows from top to bottom describe the number of observations, probability density function (PDF), CDF, and average FRP contribution respectively. The (*left column*) shows the statistics from uncorrected gridded-FRP on a 1° grid; and the (*right column*) shows the statistics from bias corrected gridded-FRP on a 1° grid. The lowest bin, which includes the FRP = 0 observations, is omitted from the plots of PDF and CDF. The corrected gridded-FRP observations shown in this figure are used for Visible Infrared Imaging Radiometer Suite (VIIRS) comparison in the next section.

Figure 3 shows that for any given FRP bin, the number of observations decreases with increasing viewing angle with the exception of very large FRP values. At lower FRP values, the number of observations decreases rapidly with decreasing FRP magnitude. As mentioned before, the systematic shift is due to the increase in the detection threshold. The underestimation in the gridded-FRP is also evident from the offset between the frequency-distributions for different viewing angles. The amount of total FRP which corresponds to the missing detections can be estimated from the average gridded-FRP (see Figure 3).

Without correction, the average gridded-FRP in the first bin (*nadir*) and the last angular bin (*off-nadir*) are 12.1 MW and 6.1 MW respectively. After correction, the distribution of the *off-nadir* gridded-FRP observations is shifted towards the nadir distribution, and the general offset between them is removed (Figure 3). The corrected PDF and the CDF also become independent of the viewing angle. As the bias correction does not extrapolate to the "false zero" FRP observations, the frequency distribution and PDF still retain their late onset of maximum.

3.4. Validation of MODIS Aqua against VIIRS Suomi-NPP

3.4.1. General Comparison

Almost similar equatorial crossing times of the Aqua MODIS and Suomi-NPP VIIRS instruments facilitate a direct comparison of the fire signals observed by the two instruments. Figure 4a shows the number of co-located fire detections (FRP pairs) grouped according to the viewing angle of

MODIS/Aqua. The number of co-located fire detections between the two satellites decreases by almost 87% from nadir to the swath edge. At the same time, the average gridded-FRP shown in Figure 4b increases towards the swath edge. These systematic effects are consistent with only larger fires being detected by MODIS and thus being included in the co-locations set for larger MODIS viewing angles. Among the co-located MODIS-VIIRS FRP pairs, VIIRS gridded-FRP observations are slightly larger than the uncorrected MODIS gridded-FRP observations at nadir (Figure 4b). This might be due to a slightly lower detection threshold of VIIRS.
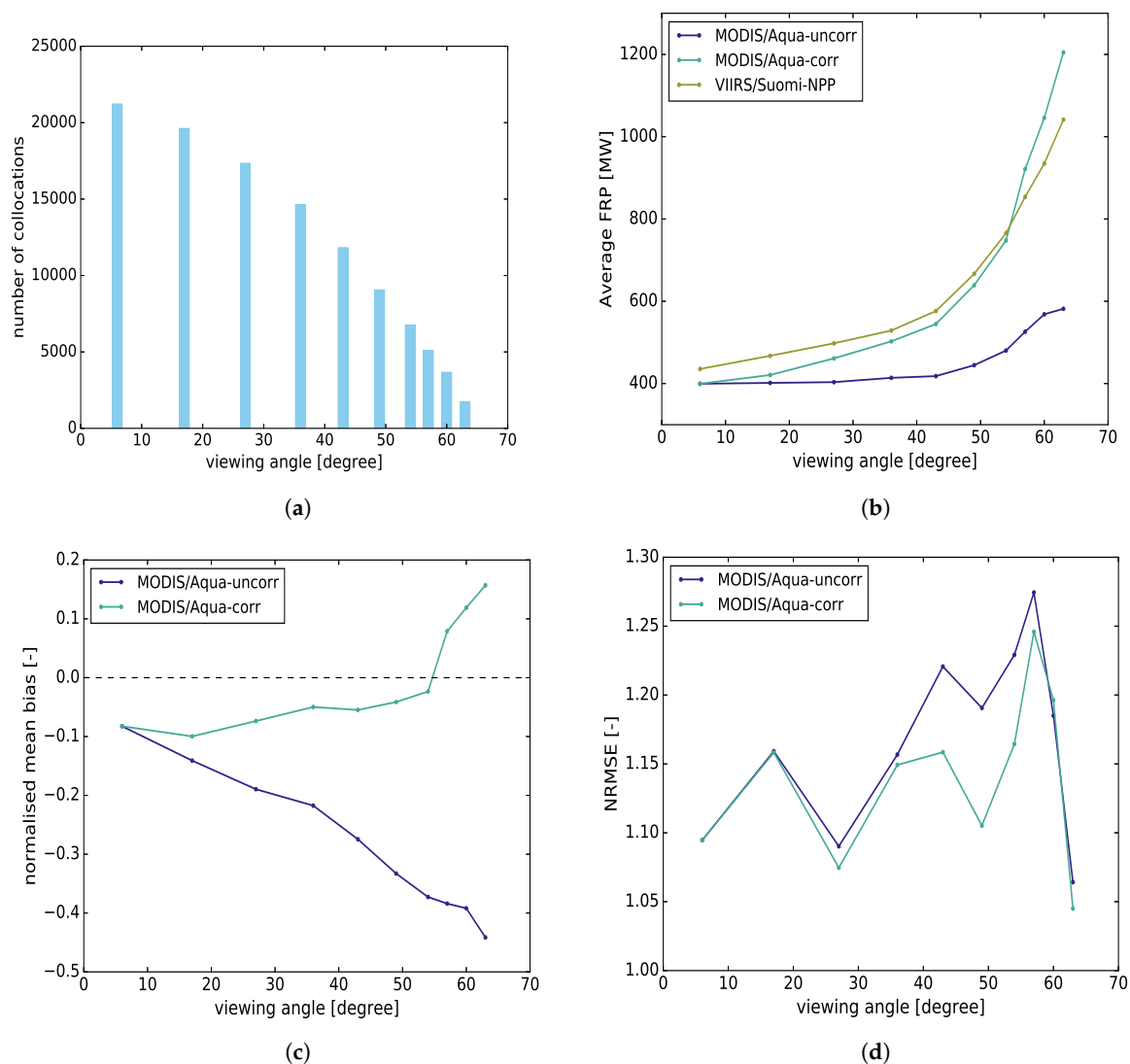

Figure 4. Statistics of co-located MODIS/Aqua and VIIRS/Suomi National Polar-orbiting Partnership (Suomi-NPP) gridded-FRP observations (hourly, 2017), with and without correction of MODIS observations, classified according to the viewing angle. (**a**) The total number of collocations between MODIS/Aqua and VIIRS/Suomi-NPP; (**b**) the average FRP per grid cell (gridded-FRP) of the co-located pairs; (**c**) the normalised mean bias between the co-located pairs (MODIS-VIIRS); (**d**) the normalised root mean square error (NRMSE) between the co-located observations.

For viewing angles up to 23°, the average difference between VIIRS and MODIS pairs is constant at about 50 MW, and the correlation between the two is also around 0.87 (Table 2). However, in the viewing angle bin with the largest viewing angle, the MODIS average gridded-FRP is only 50% of the VIIRS average gridded-FRP, and the correlation between the two drops to 0.76. After correction of MODIS gridded-FRP, the average gridded-FRP from the co-located pairs is comparable for all viewing

angles, and the correlation in each angular bin is slightly improved. The match is also evident from the normalised mean bias values (Figure 4c). For viewing angles < 55°, the bias between the co-located pairs is close to zero, but it increases rapidly at viewing angles > 55°. Interestingly, the effect of bias correction shows maximum improvement in NRMSE for gridded-FRP observations with viewing angles between 35° and 55° (Figure 4c).

The higher uncertainty associated with VIIRS gridded-FRP observations at the swath edge is an additional factor contributing to the higher discrepancy between MODIS/Aqua and VIIRS gridded-FRP co-locations for viewing angles > 55°. The on-board VIIRS pixel aggregation scheme maintains the VIIRS pixel size around 1 km^2 but towards the swath edges the pixel size reaches up to 2 km^2 [23].

Table 2. The correlation coefficient (r) between (un)corrected MODIS/Aqua and VIIRS/Suomi-NPP 1° gridded-FRP collocated pairs, grouped according to the MODIS viewing angle. The data is from the year 2017.

Viewing Angle Interval	r uncorr-MODIS	r corr-MODIS
0°–12.0°	0.88	0.88
12.0°–23.1°	0.86	0.86
23.1°–32.6°	0.88	0.88
32.6°–40.4°	0.85	0.85
40.4°–46.8°	0.84	0.85
46.8°–51.9°	0.83	0.84
51.9°–56.1°	0.79	0.80
56.1°–59.6°	0.76	0.77
59.6°–62.4°	0.76	0.77
62.4°–64.8°	0.76	0.77

3.4.2. Land Cover Type

Figure 5 shows the normalized mean bias and NRMSE statistics, according to the land cover type, for uncorrected and corrected MODIS/Aqua gridded-FRP observations co-located with VIIRS gridded-FRP observations. The co-locations with viewing angles < 55° are considered to exclude the data with higher uncertainty. The number of all co-locations per land cover type is given in Figure 5a near the zero bias line. The number of co-locations over savanna (62,939 observations) are approximately 2/3 of the total MODIS-Aqua/VIIRS-Suomi co-locations, followed by tropical forests (17,460) and agricultural land (10,553). The gridded-FRP among savanna grassland fires is consistently underestimated by uncorrected MODIS in comparison to its VIIRS counterparts. After bias correction, the normalised mean bias reduces from −0.22 to −0.08 (Figure 5b).

Over tropical forests, MODIS/Aqua sees an average gridded-FRP of 429.53 MW in contrast to 551.53 MW seen by VIIRS/Suomi-NPP. The negative normalized mean bias reduces by almost 83% after bias adjustment in MODIS/Aqua, while the NRMSE improves by approximately 6%. For both savanna and tropical forests, the VIIRS observations are consistently larger in magnitude throughout the peak burning seasons, though the bias is higher over larger viewing angles. The maximum improvement for savanna and tropical forests is observed for viewing angles between 30°–55°.
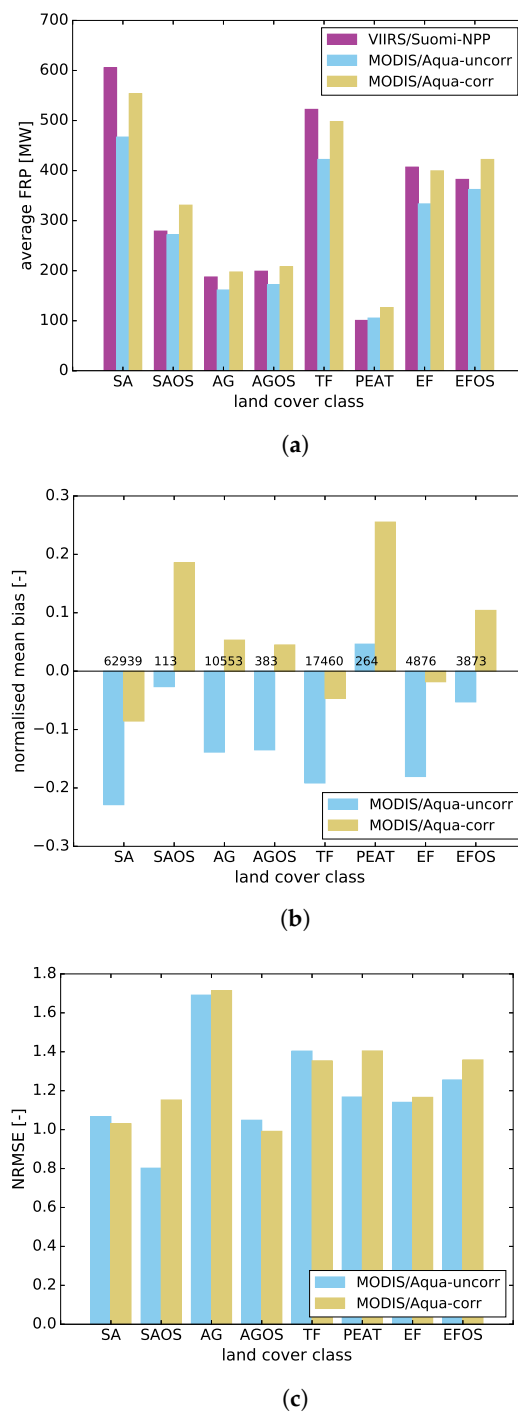
(**a**)

(**b**)

(**c**)

Figure 5. Statistics between co-located MODIS/Aqua and VIIRS/Suomi-NPP gridded-FRP observations (hourly, 2017) with and without correction, and classified according to the land cover type. (**a**) The average gridded-FRP of MODIS and VIIRS co-located pairs; (**b**) the normalized mean bias between MODIS and VIIRS co-locations. The number of co-locations for each landcover class are mentioned near the zero-bias line; (**c**) the normalized root mean square error (NRMSE) between the co-located pairs. The co-location pairs with MODIS viewing angle greater than 55° are excluded in these statistics. The labels "corr" and "uncorr" refer to MODIS/Aqua gridded-FRP observations with and without bias correction. The land cover classes used to aggregate the VIIRS/Suomi-NPP and MODIS/Aqua FRP co-location pairs, for comparison according to the fire type: savanna (SA), savanna with organic soil (SAOS), agriculture (AG), agriculture with organic soil (AGOS), tropical forest (TF), peat (PEAT), extra-tropical forest (EF), and extra-tropical forest with organic soil (EFOS) [2].

For all type of agricultural fires (AG, AGOS), MODIS and VIIRS have 10,936 concurrent detections. These observations mostly belong to the agricultural land clearing practices occurring mostly in April-May and July-October in Europe (Ukraine and surroundings), Russia and parts of southeast China and India. Among the collocations, the average gridded-FRP for VIIRS, uncorrected MODIS/Aqua, and corrected MODIS/Aqua are 198.70 MW, 166.05 MW, and 216.5 MW, respectively.

On a local scale, the magnitude of VIIRS gridded-FRP observations is consistently higher than its paired MODIS/Aqua gridded-FRP observations. After bias adjustment, a reduction in the differences is observed, e.g., over southeast Asia the normalized mean bias reduces from −0.27 to −0.12, while over southeast China and Ukraine, the normalized mean bias reduces from −0.15 to 0.03 and −0.10 to 0.09, respectively. For South American agricultural fires, we observe that MODIS gridded-FRP are larger in magnitude than their VIIRS counterparts, and after bias adjustment, the differences increase further. The average gridded-FRP among the collocation pairs over South America is 264 MW for VIIRS and 308 MW for uncorrected MODIS-Aqua. The negative bias between uncorrected MODIS/Aqua and VIIRS/Suomi-NPP collocations for agricultural fires over the whole globe but South America is mostly due to two reasons: underestimation in the uncorrected MODIS gridded-FRP, and larger number of small fire detections by VIIRS that leads to a higher FRP estimate at a 1° grid. The exceptional behaviour over South American agricultural fires can be attributed to the improper classification of the fire regimes. The South American agricultural fires exist in fragments among savanna and tropical forest biomes and commonly lead to accidental spreads.

Studies show that land cover class often fails in delineating the different fire regimes [26,27]. When the observations over South America are excluded from the agricultural class, the average gridded-FRP for VIIRS, uncorrected MODIS-Aqua, and corrected MODIS-Aqua gridded-FRP observations are approximately 170 MW, 141 MW, and 172 MW respectively. The normalized mean bias between the uncorrected MODIS and VIIRS gridded-FRP observations is −0.135, while after correction it reduces to 0.045. Similarly, the NRMSE reduces from 1.04 to 0.99.

Boreal forests (EFOS) account for around 4% (3873) of co-located VIIRS/Suomi-NPP and MODIS/Aqua gridded-FRP observations. Most fires are observed in Eurasia from June–August. The average gridded-FRP is 382 MW for VIIRS, 362 MW for uncorrected MODIS/Aqua, and 422 MW for corrected MODIS/Aqua. Previously in the literature [17,28], the authors have described that the massive smoke plumes from boreal forests can affect the FRP signal in both MODIS and VIIRS NIR band, though the effect is more pronounced in VIIRS due to wider NIR band. The attenuation of the VIIRS signal leads to lower estimates in the VIIRS per pixel FRP observations in comparison to the MODIS per-pixel observations. If we look at the VIIRS/MODIS collocations with MODIS viewing angle $< 25°$, the average gridded-FRP among collocations is 371 MW for VIIRS, while for MODIS the average FRP is 377 MW. After bias correction, the magnitude of MODIS average gridded-FRP is larger than their VIIRS counterparts (Figure 5a).

Among the gridded-FRP observations belonging to extra-tropical forests, more than half of the VIIRS-NPP/MODIS-Aqua collocations are from North America temperate forest fires, and the rest are contributions from similar biomes around the world. The co-located, uncorrected MODIS-Aqua average gridded-FRP is 333 MW, while the average of VIIRS gridded-FRP is 407 MW. After correction, the magnitudes of co-located VIIRS and MODIS-Aqua pairs are comparable. The mean bias reduces to −8 MW and the corresponding normalized mean bias reduces from −0.16 to −0.02, though NRMSE values do not show any change. Among the 264 contemporaneous FRP detections of peat fires by VIIRS and MODIS-Aqua, the magnitude of uncorrected MODIS-Aqua gridded-FRP observations is almost comparable to VIIRS gridded-FRP observations (Figure 5). The average gridded-FRP for uncorrected Aqua and VIIRS are 105 MW and 100 MW. After bias correction, the differences between the two increase and the NRMSE also increases. The high uncertainty associated with the peat fire detections and low number of collocations (0.02% of total collocations) makes it hard to conclude any specific trend between the two satellites.

3.5. Comparison of GFAS Analyses

To analyse the performance of all four experiments with GFAS, the fire radiative energies (FRE) over various regions around the globe are compared. The daily FRE is the temporal integration of the fire radiative power over the whole day. The daily FRE computed for each of the ten regions is plotted in Figure 6.
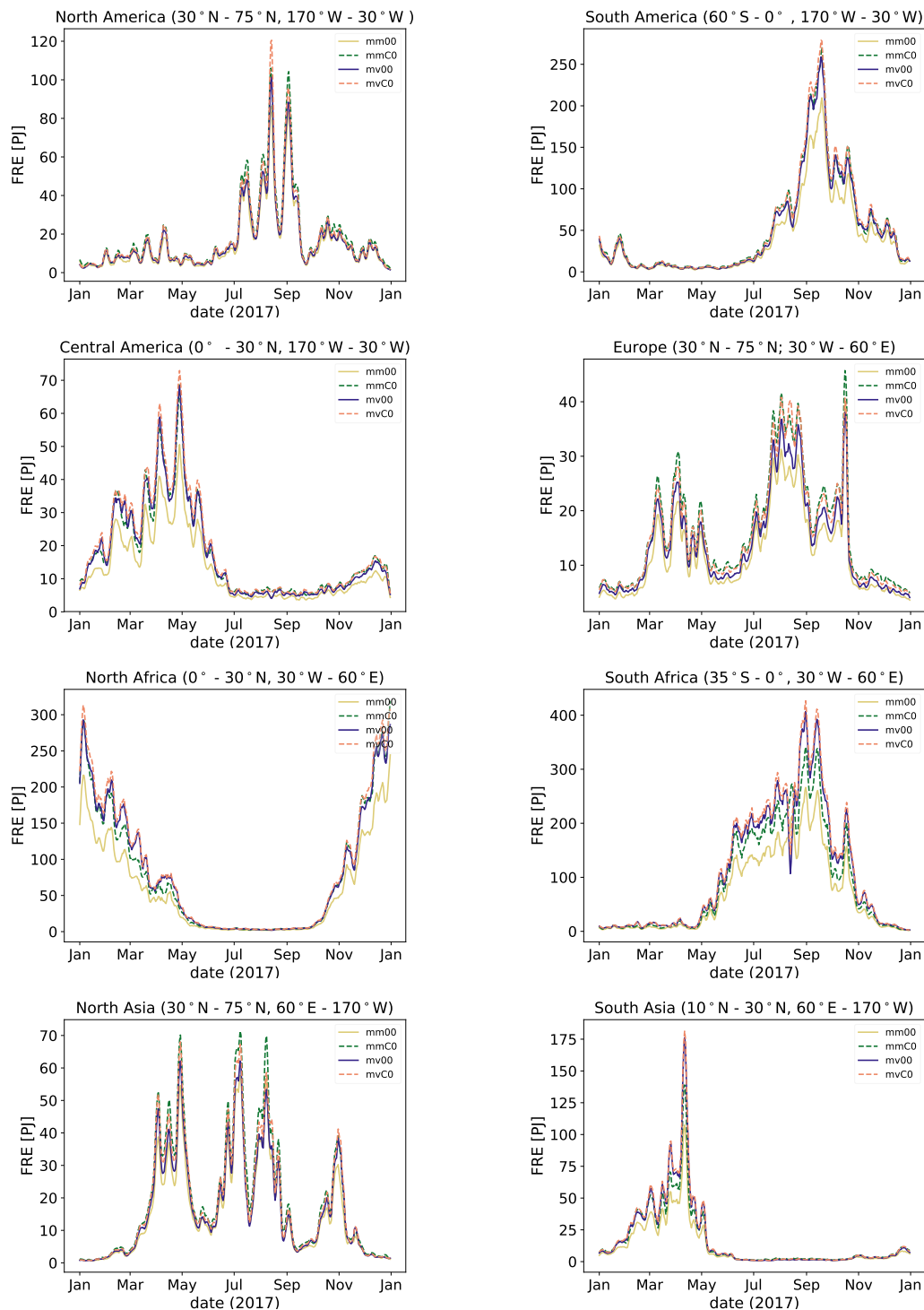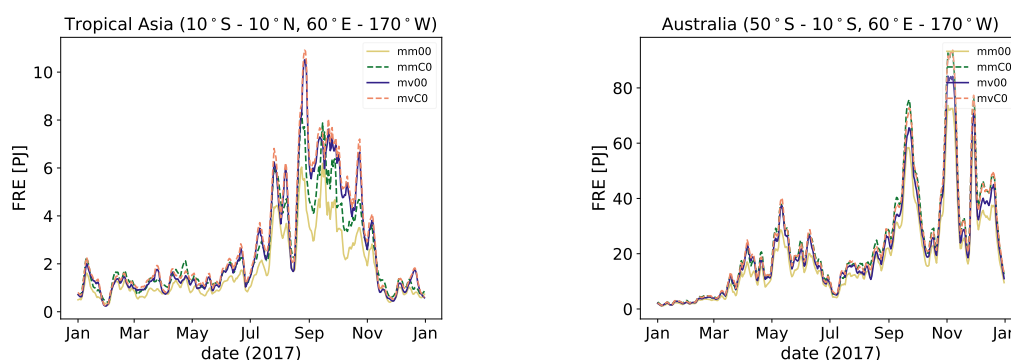

Figure 6. *Cont.*

Figure 6. The subfigures show the daily fire radiative energy (FRE) of 2017 as estimated from different experiments with Global Fire Assimilation System (GFAS) over several regions around the globe. The region name and the latitude/longitude extent are described in the title of each sub-figure. The details of the experiments: mm00: Uncorrected gridded-FRP from MODIS/Aqua and MODIS/Terra are used as input. mv00: Uncorrected gridded-FRP from MODIS/Terra and VIIRS/Suomi-NPP are used as inputs. VIIRS/Suomi-NPP is used as a replacement for MODIS/Aqua. mmC0: Corrected gridded-FRP from both MODIS/Aqua and MODIS/Terra are used as inputs. mvC0: Corrected gridded-FRP from MODIS/Terra and gridded-FRP from VIIRS/Suomi-NPP are used as inputs. See also Table 1.

The annual FRE over each region is also given in Table 3. The regional differences between the different experiments are described as follows:

North America: The FRE from fires in North America is about 5% of the global FRE budget. During the peak boreal forest burning season (July to September), the FRE in experiment MOD-& MYD-uncorrected' ('mm00') is 3162.7 PJ, while after correction ('mmC0'), it increases to 3941.01 PJ. In the experiment 'MOD & VNP' ('mv00') the FRE during this period is 3446.73 PJ, while with VIIRS and corrected Terra gridded-FRP observations ('mvC0') it is 3815.52 PJ.

Central America & South America: Fires in Central and South America contribute about 5% and 14% to the annual FRE. Over both regions, the FRE estimates in all four experiments: 'uncorrected MOD-& MYD' ('mm00'), 'MOD-& MYD-corrected' ('mmC0'), 'uncorrected MOD & VNP'('mv00'), and 'MOD-corrected & VNP'('mv00') are 19135.1 PJ, 25106.9 PJ, 24041.5 PJ, and 26207 PJ, respectively. In the South American peak burning season (August to November), the daily FRE estimates from experiment 'MOD-corrected & VNP' ('mvC0') and 'MOD-&MYD-corrected' ('mm00') differ by approximately 5.5 PJ. Similar results are obtained for Central America where the peak burning season (March to May) is also dominated by tropical and savanna fires. The daily FRE estimates during this period from experiment 'MOD-corrected & VNP' ('mvC0') and 'MOD &MYD-corrected' ('mm00') differ by approximately 4 PJ. Over both regions, a higher FRE is observed in experiments using VIIRS gridded-FRP observations ('mv00', 'mvC0').

North Africa and South Africa: The savanna fires over Northern Africa and Southern Africa are the major contributors to the global FRE budget. The energy release from fires in Northern Africa and Southern Africa are approximately 23% and 30% respectively. The magnitude of the FRE released in the peak burning savanna season (November to February) for 'MOD- & MYD-uncorrected' ('mm00') is lower than experiment 'MOD-& MYD-corrected' ('mm00') by 5543.3 PJ. However, the FRE estimates from MOD- & VNP-corrected ('mvC0') are 1849.14 PJ higher than the experiment MOD-&MYD-corrected ('mm00'). The average daily FRE difference between the two is approximately 15 PJ. A similar trend is also observed over southern hemisphere Africa peak burning season (July to September). In Southern Africa, during the peak burning season (November to February), the FRE estimate in GFAS experiment 'mvC0' is 5132 PJ higher than GFAS experiment 'mm00', indicating that the VIIRS gridded-FRP observations have a stronger impact on GFAS analyses.

Europe: From March to April, the dominant contributor to the FRE estimates are agricultural burns in Eastern Europe. During this period, the FRE from bias-corrected MODIS FRP observations ('mmC0') and VIIRS gridded-FRP observations ('mvC0') is 1177.65 PJ and 1131.55 PJ. In July, the FRE estimates from experiments 'mmC0' and 'mvC0' are 803.4 PJ and 765.3 PJ respectively, but in August the FRE from the experiment corrected MODIS-Aqua gridded-FRP observation ('mmC0') is 1089.3 PJ, but in the experiment VIIRS FRP observations ('mvC0') the FRE is 1093.3 PJ.

North Asia: The energy release from Northern Asia forms approximately 5% of the global FRE budget. During the peak burning period (June to September), the FRE in experiment 'mm00' is 247.1 PJ higher than 'mvC0'. But from October–November, the period dominated by agricultural fires and Mongolian grassland fires, the average bias between daily FRE from experiment 'mmC0' and experiment 'mvC0' is approximately 3 PJ. The period from March to May is also dominated by the agricultural and grassland fires, but the large values of FRE in May suggests a contribution from scattered boreal fires just before the beginning of the peak burning season.

Tropical and South Asia: Over tropical Asia, the FRE from experiments 'MOD-&MYD uncorrected' ('mm00') and 'MOD-&MYD corrected' ('mmC0') are 640.8 PJ and 866.7 PJ, respectively. During the peak burning season over Tropical Asia (August to October), the daily FRE from the experiment 'MOD-corrected&VNP' (mvC0) is approximately 1.26 PJ higher than the experiment 'MOD-&MYD-corrected'('mmC0'). A similar effect is also observed over the South Asian peak burning sesaon (March to May), where the daily FRE from the corrected MODIS observations is approximately 9 PJ higher than the experiment using uncorrected MODIS gridded-FRP observations ('mm00'). However, the average daily FRE difference between experiments 'mVC0' and 'mmC0' is also around 9 PJ, indicating a higher impact of the VIIRS observations.

Australia: The FRE from Australian bushfires in the experiment 'MOD-&MYD uncorrected' ('mm00') is only 6699.8 PJ, however after bias correction ('mmC0'), the FRE increases to 8638.7 PJ. This is comparable to the GFAS experiment 'mVC0', where the input of corrected Terra gridded-FRP observations and VIIRS gridded-FRP observations results in an annual FRE of 8595.2 PJ.

Table 3. The annual Fire Radiative Energy (FRE) of 2017 (in PJ) from all four experiments (Table 1) for all regions. Abbreviations mv00: Uncorrected gridded-FRP from MODIS/Terra and VIIRS/Suomi-NPP are used as input. VIIRS/Suomi-NPP is used as a replacement for MODIS/Aqua. mmC0: Corrected gridded-FRP from both MODIS/Aqua and MODIS/Terra are used as input. mvC0: Corrected gridded-FRP from MODIS/Terra and gridded-FRP from VIIRS/Suomi-NPP are used as input.

Region	FRE-mm00 (PJ)	FRE-mmC0 (PJ)	FRE-mv00 (PJ)	FRE-mvC0 (PJ)
N. America	5519.2	6946.5	6057.6	6648.9
C. America	4762.7	6377.0	6331.2	6883.2
S. America	14,372.4	18,729.9	17,710.3	19,323.8
Europe	4404.8	5914.4	5085.9	5682.0
N. Africa	20,425.6	27,454.6	28,750.3	30,560.9
S. Africa	25,283.5	33,113.4	38,416.6	40,522.5
N. Asia	5589.8	7135.9	6139.9	6728.9
S. Asia	4323.1	5685.5	6265.3	6594.2
T. Asia	640.8	866.7	936.1	1010.1
Australia	6698.8	8638.8	7832.4	8595.2

The energy release over all continental regions is dominated by the seasonal biomass burning in each region. Among all experiments, the FRE values are lowest in MOD- & MYD-uncorrected ('mm00'). The difference is highest during the peak burning season, while the magnitude of energy release in other three experiments ('mv00', 'mmC0', 'mvC0') varies according to the regions. The energy release from boreal fires in North America and North Asia is smaller when VIIRS gridded-FRP observations are assimilated. There may be an underestimation of VIIRS gridded-FRP observations over boreal forests due to infrared signal attenuation in the atmosphere, which has already been described in the previous section. Among other land-cover types, regional differences in the energy release are observed

over tropics. A larger number of detections by VIIRS over tropical regions [23,28] is a dominant factor towards the higher FRE in GFAS experiments with VIIRS FRP input.

4. Conclusions

The detection threshold of the MODIS instruments increases with viewing angle and pixel size towards the swath edges. For example, for savanna as a dominant fuel type, the detection threshold varies by a factor of eight from nadir to the swath edge [8]. Hence, small fires with magnitude less than the detection threshold cannot be detected. When MODIS per-pixel FRP observations are converted to a gridded representation like GFAS, the missing fire detections lead to lower FRP estimates in grid cells observed with large viewing angles. Additionally, the isolated missing fires also lead to "false zero" FRP grid cells. These effects introduce erroneous fluctuations in FRP magnitude, which propagate to pyrogenic emission inventories and atmospheric composition models.

In this study, we describe a quantile mapping (QM)-based technique to remove the systematic negative bias in the gridded representation of MODIS FRP observations. QM is a common procedure to correct the biases associated with modelled quantities in comparison to observations. QM maps the cumulative distribution function (CDF) of the uncorrected quantities to that of a reference and derives the respective correction factors for bias removal.

The application of QM to gridded-FRP observations is based on the assumption that, when a sufficiently long sampling period is chosen, the variable overpass geometry of the MODIS instruments ensures that virtually identical fire distributions are sampled at all viewing angles. In this study, we select the *near-nadir* FRP distribution (viewing angle < 12°) as reference, and derive the correction factors for the off-nadir viewing angles. The correction factors are characterised by the FRP magnitude and the viewing angle. In this method, the contribution of isolated missing fires is not corrected directly, but their contribution is added to other non-zero grid cells in the vicinity. The FRP magnitude in the observed grid cells is increased in order to account for the contribution of missing fires.

We show that this approach works best when the correction factors are derived on a coarser grid than 0.1° resolution. We find 1° resolution to be a reasonable choice: without any bias correction, the FRP estimates for grid cells with viewing angle greater than 55° are underestimated by more than 50%. After bias correction with 0.1° correction factors, the fraction of uncorrected FRP near the swath edges is almost 30%. However, with 1° correction factors, the residual missing FRP is only 6%. This residual missing FRP after bias correction is mostly the contribution of isolated "false zero" grid cells that cannot be corrected. Reducing the spatial resolution further than 1° does not introduce any significant changes in the bias reduction. Hence to avoid any unnecessary loss of spatial information, we suggest 1° resolution for deriving the bias correction factors. At this resolution (1°) the contribution of the missing fire detections is added to observed fires with up to approximately 100 km distance. However, when the 1° correction factors are applied to a finer-scale gridded-FRP field, e.g., 0.1°, the FRP in the grid cells with fire detections is somewhat overestimated in order to compensate for missing fire detections in neighbouring grid cells at up to 100 km distance.

Due to a lack of ground-based FRP observations for a direct validation of the bias-corrected gridded-FRP, we compare co-located MODIS/Aqua and VIIRS/Suomi-NPP fire detections to evaluate the performance of the correction procedure. Almost similar equatorial crossing times of Aqua and Suomi-NPP offer a direct comparison between the two. The per-pixel FRP observations from both satellites are gridded on 1° GFAS grid and are compared globally and according to the land-cover type.

On a global scale, the comparison of the corrected MODIS/Aqua gridded-FRP and VIIRS gridded-FRP shows a good match for viewing angles < 55°. The relationship between the two on regional scales depends upon the land-cover type, though. The bias between VIIRS and MODIS co-locations with 55° MODIS viewing angle is reduced from ∼ 163 MW to ∼ 19 MW after correction.

Analyses according to the land cover type show that MODIS/Aqua gridded-FRP observations over savannas and tropical forests are always underestimated with respect to VIIRS. After bias correction, the average FRP over both biomes is comparable. The broadleaf forest fires in the two

satellites products are also comparable after correction, but for boreal fires, the magnitude of VIIRS observations is usually lower. This may be caused by a systematic underestimation of VIIRS at boreal forests rather than errors in the corrected MODIS-Aqua gridded-FRP. The VIIRS FRP underestimation at boreal forests has been ascribed to CO_2 attenuation by Li et al. [28]. The lack of land-cover type information in the correction factors can also lead to an unexpected overestimation in regions where multiple biomes exist in close proximity. For example, in South America, the agricultural fires often exist in fragments within tropical forest fires. When a $1°$ grid cell in this region is corrected according to its magnitude, the contribution of missing low-intensity agricultural fires can be added to tropical fires which are much higher in magnitude, thus leading to overestimation. Although deriving the correction factors according to the land-cover class seems a plausible solution to this limitation, we believe that the land-cover class information on a coarser grid can introduce over-fitting in GFAS over poorly known/changing land-cover and mosaic landscapes.

The effect of corrected MODIS gridded-FRP observations is also analyzed in the GFAS inventory context. Four experiments with corrected/uncorrected MODIS gridded-FRP and VIIRS gridded-FRP as input are conducted. Using the bias-corrected MODIS observations in GFAS leads to $\sim 31\%$ increase in the annual global FRE in comparison to using uncorrected gridded-FRP. However, when VIIRS gridded-FRP are used as an replacement of MODIS/Aqua, the annual global FRE is 9% higher even than the GFAS experiment using corrected gridded-FRP from both MODIS instruments. Using VIIRS gridded-FRP instead of corrected MODIS/Aqua leads to a higher FRE budgets over tropics due to larger number of detections by VIIRS over tropical regions. The maximum difference is seen over southern hemisphere Africa where using VIIRS instead of MODIS/Aqua increases the annual FRE by 22%. The underestimation in VIIRS gridded-FRP over boreal forests is also evident in the GFAS analyses. The annual FRE over North America after using corrected MODIS gridded-FRP is 6946 PJ, but replacing MODIS/Aqua with VIIRS reduces the annual FRE to 6648 PJ.

In summary, the correction factors described in this study provide a simple yet powerful way to correct the swath-dependent bias in the MODIS gridded-FRP observations. The correction factors vary with fire magnitude and viewing angle, and thus are applicable to global gridded-FRP observation with various fire types. The uniqueness of the methodology lies in the fact that the correction factors can be applied at the level of gridded-FRP observations and are thus applicable to all existing FRP-based emission inventories like GFAS, IS4FIRES [4], and NASA's Fire Energetic and Emissions Research (FEER) [29] and Quick Fire Emissions Database (QFED) [6]. Reducing the swath dependence of FRP observation is crucial for an accurate representation of the variability of emissions in transport models and hence regional and global air quality monitoring. In the future, as VIIRS and SLSTR FRP observations replace the MODIS FRP observations, bias correction of the MODIS FRP observations will allow a smooth transition from MODIS to VIIRS and SLSTR in existing applications.

In the future, the presented bias correction technique can be applied to geostationary observations. There is even a potential to apply the correction functions directly with the parameters derived for MODIS to other satellites by translating the viewing angles to the corresponding pixel footprint sizes of the different satellite instruments and implementing a universal correction factor that depends only on pixel size and fire magnitude.

and VIIRS active fire data. The data was downloaded from https://earthdata.nasa.gov/earth-observation-data/near-real-time/firms/active-fire-data.

Conflicts of Interest: The authors declare no conflict of interest.

Appendix A.

Table A1. Definitions of various FRP variants used in the article.

FRP Variant	Description	Units
per-pixel FRP	The singular value of FRP associated with an individual active fire pixel from MODIS/VIIRS instruments	W
FRP areal density	The average FRP emitted over the ground area subtended by the grid cell defined according to the GFAS gridding algorithm	W m^{-2}
gridded-FRP	The FRP emitted per grid cell. It is the product of the FRP areal density and the grid cell area	W
average gridded-FRP	The average of the gridded-FRP	W
FRP analyses	The best estimate of the gridded-FRP obtained from GFAS	W

Appendix B. Frequency-Magnitude Distribution of $0.1°$ **MODIS Gridded-FRP**

Figure A1 shows the statistical properties of the MODIS gridded-FRP from 2017 after correction. The gridded-FRP at $0.1°$ resolution have been corrected using correction function described by Equation (16) (derived from $1°$). The corrected gridded-FRP have been re-gridded to a $1°$ grid after correction. To coarsen the gridded-FRP observations, the FRP areal density for each grid cell is determined and summed over the coarse grid cell. The gridded-FRP of the coarse grid cell is the product of the new FRP areal density and the area of the coarse grid cell.

When the bias correction is applied at a finer, $0.1°$ resolution, it leads to a slight overestimation of the overall FRP magnitude. This effect is more pronounced for large viewing angles. The overestimation is probably an artifact of the correction factors derived at a coarser resolution. At $1°$ resolution, the correction function account for all missing fires in an approximate periphery of 100 km. But when the same correction function is used to correct the gridded-FRP on a finer scale, all non-zero $0.1°$ grid cells are corrected. When the corrected $0.1°$ grid cells are aggregated on a $1°$ grid, the total correction in a $1°$ grid cell will be slightly more than directly correcting the $1°$ grid cell. This overestimation will be highest at the swath edges. However, since there is no method to directly correct the "false zero" FRP observations, applying the bias correction, even at a finer resolution, helps in alleviating the swath dependence of MODIS gridded-FRP observations, albeit with a slight overestimation at swath edges.
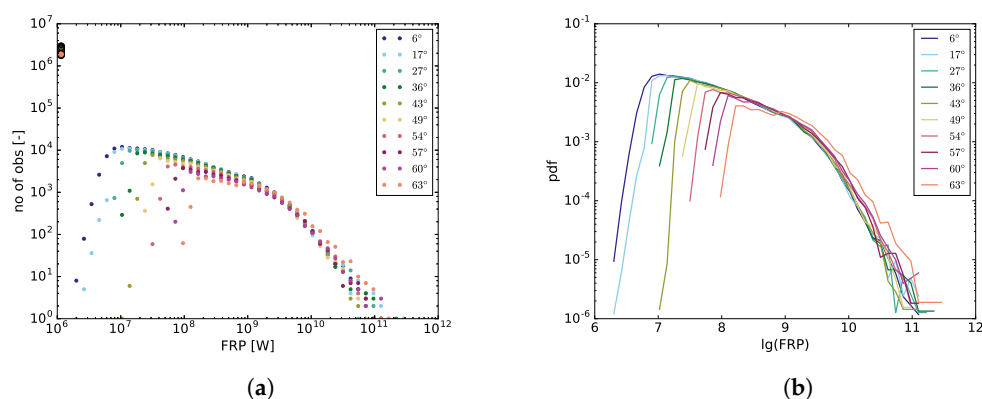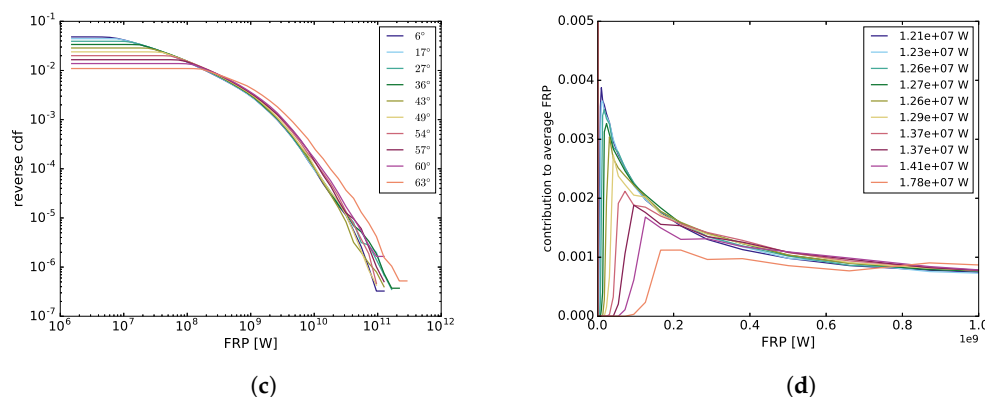

(a)   (b)

Figure A1. *Cont.*

(**c**)   (**d**)

Figure A1. Statistical properties of MODIS gridded-FRP observations (hourly, 2017) after bias correction: (**a**) number of observations, (**b**) probability density function (PDF), (**c**) "reverse" Cumulative distribution function (CDF), (**d**) contribution to average gridded FRP. The gridded-FRP with 0.1° resolution are corrected according to the correction factors described in Figure 1, and then re-gridded to 1° grid.

References

1. Justice, C.; Townshend, J.; Vermote, E.; Masuoka, E.; Wolfe, R.; Saleous, N.; Roy, D.; Morisette, J. An overview of MODIS Land data processing and product status. *Remote Sens. Environ.* **2002**, *83*, 3–15. [CrossRef]
2. Kaiser, J.W.; Heil, A.; Andreae, M.O.; Benedetti, A.; Chubarova, N.; Jones, L.; Morcrette, J.J.; Razinger, M.; Schultz, M.G.; Suttie, M.; et al. Biomass burning emissions estimated with a global fire assimilation system based on observed fire radiative power. *Biogeosciences* **2012**, *9*, 527–554. [CrossRef]
3. Kaiser, J.W.; Flemming, J.; Schultz, M.G.; Suttie, M.; Wooster, M.J. *The MACC Global Fire Assimilation System: First Emission Products (GFASv0)*; Technical Memorandum 596; European Centre for Medium-Range Weather Forecasts: Reading, UK, 2009.
4. Sofiev, M.; Vankevich, R.; Lotjonen, M.; Prank, M.; Petukhov, V.; Ermakova, T.; Koskinen, J.; Kukkonen, J. An operational system for the assimilation of the satellite information on wild-land fires for the needs of air quality modelling and forecasting. *Atmos. Chem. Phys.* **2009**, *9*, 6833–6847. [CrossRef]
5. Bloom, S.; da Silva, A.; Dee, D.; Bosilovich, M.; Chern, J.-D.; Pawson, S.; Schubert, S.; Sienkiewicz, M.; Stajner, I.; Tan, W.-W.; et al. *Documentation and Validation of the Goddard Earth Observing System (GEOS) Data Assimilation System, Version 4*; M.J. Suarez, Ed.; Technical Report Series on Global Modeling and Data Assimilation; NASA/TM-2005?104606/ VOL26/VER4; National Aeronautics and Space Administration: Washington, DC, USA, 2005.
6. Darmenov, A.; da Silva, A. *The Quick Fire Emissions Dataset (QFED)—Documentation of Versions 2.1, 2.2 and 2.4*; Koster, R. D., Ed.; NASA Technical Report Series on Global Modeling and Data Assimilations; NASA/TM-2015-104606 /Vol. 38; National Aeronautics and Space Administration: Washington, DC, USA, 2005.
7. Nishihama, M.; Wolfe, R.; Solomon, D.; Patt, F.; Blanchette, J.; Fleig, A.; Masuoka, E. *MODIS Level 1A Earth Location*; MODIS Algorithm Theoretical Basis Document Version 3.0; National Aeronautics and Space Administration: Washington, DC, USA, 1997.
8. Freeborn, P.H.; Wooster, M.J.; Roberts, G. Addressing the spatiotemporal sampling design of MODIS to provide estimates of the fire radiative energy emitted from Africa. *Remote Sens. Environ.* **2011**, *115*, 475–489. [CrossRef]
9. Zhang, T.; Wooster, M.J.; Xu, W. Approaches for synergistically exploiting VIIRS I- and M-Band data in regional active fire detection and FRP assessment: A demonstration with respect to agricultural residue burning in Eastern China. *Remote Sens. Environ.* **2017**, *198*, 407–424. [CrossRef]
10. Andela, N.; Kaiser, J.W.; Heil, A.; van Leeuwen, T.T.; Wooster, M.J.; van der Werf, G.R.; Remy, S.; Schultz, M.G. *Assessment of the Global Fire Assimilation System (GFASv1)*; Technical Memorandum 702; European Centre for Medium-Range Weather Forecasts: Reading, UK, 2013.

11. Saide, P.E.; Peterson, D.A.; da Silva, A.; Anderson, B.; Ziemba, L.D.; Diskin, G.; Sachse, G.; Hair, J.; Butler, C.; Fenn, M.; et al. Revealing important nocturnal and day-to-day variations in fire smoke emissions through a multiplatform inversion. *Geophys. Res. Lett.* **2015**, *42*, 3609–3618. [CrossRef]

12. Andela, N.; van der Werf, G.R.; Kaiser, J.W.; van Leeuwen, T.T.; Wooster, M.J.; Lehmann, C.E.R. Biomass burning fuel consumption dynamics in the tropics and subtropics assessed from satellite. *Biogeosciences* **2016**, *13*, 3717–3734. [CrossRef]

13. Wang, J.; Yue, Y.; Wang, Y.; Ichoku, C.; Ellison, L.; Zeng, J. Mitigating satellite-based fire sampling limitations in deriving biomass burning emission rates: Application to WRF-Chem model over the Northern Sub-Saharan African region. *J. Geophys. Res. Atmos.* **2018**, *123*, 507–528. [CrossRef]

14. Zhang, T.; Wooster, M.J.; De Jong, M.C.; Xu, W. How Well Does the Small Fire Boost Methodology Used within the GFED4.1s Fire Emissions Database Represent the Timing, Location and Magnitude of Agricultural Burning? *Remote Sens.* **2018**, *10*, 823. [CrossRef]

15. Kaiser, J.; Andela, N.; Atherton, J.; de Jong, M.; Heil, A.; Paugam, R.; Remy, S.; Schultz, M.; van der Werf, G.; van Leeuwen, T.; et al. *Recommended Fire Emission Service Enhancements*; Technical Memorandum 724; European Centre for Medium-Range Weather Forecasts: Reading, UK, 2014.

16. Giglio, L.; Schroeder, W.; Hall, J.V.; Justice, C.O. *MODIS Collection 6 Active Fire Product User's Guide Revision B*; National Aeronautics and Space Administration: Washington, DC, USA, 2018.

17. Giglio, L.; Schroeder, W.; Justice, C.O. The collection 6 MODIS active fire detection algorithm and fire products. *Remote Sens. Environ.* **2016**, *178*, 31–41. [CrossRef] [PubMed]

18. Nikonovas, T.; Wooster, M.; Xu, W.; He, J.; Kaiser, J.W. *Methodology to Grid Pixel FRP Data From MODIS and SEVIRI Satellite Products: Development Report*; Technical Report CAMS44_2016SC1_D3.1.1.a-2016_201612_v1; Copernicus Atmosphere Monitoring Service: Brussels, Belgium, 2016.

19. Cannon, A.J.; Sobie, S.R.; Murdock, T.Q. Bias Correction of GCM Precipitation by Quantile Mapping: How Well Do Methods Preserve Changes in Quantiles and Extremes? *J. Clim.* **2015**, *28*, 6938–6959. [CrossRef]

20. Thrasher, B.; Maurer, E.P.; McKellar, C.; Duffy, P.B. Technical Note: Bias correcting climate model simulated daily temperature extremes with quantile mapping. *Hydrol. Earth Syst. Sci.* **2012**, *16*, 3309–3314. [CrossRef]

21. Piani, C.; Haerter, J.O.; Coppola, E. Statistical bias correction for daily precipitation in regional climate models over Europe. *Theor. Appl. Climatol.* **2010**, *99*, 187–192. [CrossRef]

22. Kaiser, J.W.; Heil, A. *Description of FRP Product Consistency Monitoring System : Development Report*; Technical Report CAMS44_2016SC1_D44.3.2.1.b_201711_Description_of_FRP_Product_Consistency_Monitoring_System_0; Copernicus Atmosphere Monitoring Service: Brussels, Belgium, 2016.

23. Wolfe, R.E.; Lin, G.; Nishihama, M.; Tewari, K.P.; Tilton, J.C.; Isaacman, A.R. Suomi NPP VIIRS prelaunch and on-orbit geometric calibration and characterization. *J. Geophys. Res. Atmos.* **2013**, *118*, 11,508–11,521. [CrossRef]

24. Zhang, T.; Wooster, M.; Xu, W.; Kaiser, J.W. *Methodology to Grid Pixel FRP Data From VIIRS Products and Produce Gridded FRP Error Estimates*; Technical Report CAMS44_2016SC3_D44.3.1.2.a-2018; Copernicus Atmosphere Monitoring Service: Brussels, Belgium, 2018.

25. Van der Werf, G.R.; Randerson, J.T.; Giglio, L.; Collatz, G.J.; Mu, M.; Kasibhatla, P.S.; Morton, D.C.; DeFries, R.S.; Jin, Y.; van Leeuwen, T.T. Global fire emissions and the contribution of deforestation, savanna, forest, agricultural, and peat fires (1997–2009). *Atmos. Chem. Phys.* **2010**, *10*, 11707–11735. [CrossRef]

26. Chuvieco, E.; Giglio, L.; Justice, C. Global characterization of fire activity: toward defining fire regimes from Earth observation data. *Glob. Chang. Biol.* **2008**, *14*, 1488–1502. [CrossRef]

27. Giglio, L.; Csiszar, I.; Justice, C.O. Global distribution and seasonality of active fires as observed with the Terra and Aqua Moderate Resolution Imaging Spectroradiometer (MODIS) sensors. *J. Geophys. Res. Biogeosci.* **2006**, *111*. [CrossRef]

28. Li, F.; Zhang, X.; Kondragunta, S.; Csiszar, I. Comparison of Fire Radiative Power Estimates From VIIRS and MODIS Observations. *J. Geophys. Res. Atmos.* **2018**, *123*, 4545–4563. [CrossRef]

29. Ichoku, C.; Ellison, L. Global top-down smoke aerosol emissions estimation using satellite fire radiative power measurements. *Atmos. Chem. Phys. Discuss.* **2013**, *13*, 27327–27386. [CrossRef]